Available online at www.sciencedirect.com
SCIENCE DIRECT®
Journal of Computational Physics 199 (2004) 150–174
JOURNAL OF COMPUTATIONAL PHYSICS
www.elsevier.com/locate/jcp

A shock-capturing wave-propagation method for dry and saturated granular flows

P. Vollmöller *

Laboratoire d'Hydraulique Environnemental ENAC, EPFL-Lausanne, CH-1015 Lausanne, Switzerland

Received 2 October 2003; received in revised form 5 February 2004; accepted 6 February 2004
Available online 19 March 2004

Abstract

The Savage–Hutter (SH) equations for dry granular flows are a system of hyperbolic balance laws which is based on a Coulomb friction approach for the description of internal failure and basal sliding and determines the time-dependent behaviour of depth and depth-integrated velocity components in a terrain following coordinate system (tangential to the sliding bed). Alternatively the Iverson–Denlinger (ID) equations are a system of hyperbolic balance laws for the determination of the time-dependent behaviour of fluid-saturated granular flows. They are based on the SH-theory, explicitly consider the fluid phase using a two-phase approach, but do not correspond with the SH-theory in the cases of a vanishing fluid phase. Important terms originating from the kinematic bottom boundary condition and taking care of the variable bed slope are neglected and a term taking the internal failure into account was added. In this paper I present a new numerical method, a wave-propagation method for the solution of the SH- and the ID-equations. It works in the finite volume context and uses Godunov-type schemes with spatially discretized flux functions. Since the SH-equation as well as the ID-equations are balance laws, the source terms are taken into account in form of adapted flux differences before the wave decomposition is performed. A first order as well as a second order version are derived. They are compared with the classical fractional-step or operator-splitting method for the solution of balance laws, which serves as a reference method. Both methods are applied on several test problems: (1) a dry granular flow in a rectangular flume with a bed surface inclination of $\Theta = 31.4°$, (2) a dry granular flow in a rectangular flume ($\Theta = 40°$), (3) a dry granular flow down an inclined plane ($\Theta = 31.4°$), (4) a dry granular flow down an inclined plane diverted by an obstacle ($\Theta = 40°$) and (5) a fluid-saturated granular flow down an inclined plane ($\Theta = 31.4°$).

Keywords: Granular flows; Shock-capturing; Wave-propagation method; Fractional-step method; Free moving boundary

1. Introduction

Granular flows occur when inhomogeneous sediment–air mixtures move down steep slopes or channel-shaped regions in response to gravitational acceleration. The deformation of dry granular materials takes

* Tel.: +41-(0)21-6934362.
E-mail address: peter.vollmoeller@epfl.ch (P. Vollmöller).

0021-9991/$ - see front matter © 2004 Elsevier Inc. All rights reserved.
doi:10.1016/j.jcp.2004.02.008

place in a slow tranquil mode characterized by enduring frictional grain contacts. Their rapid agitated flows are characterized by brief inelastic grain collisions. In contrast to the dry granular flows there are the fluid-saturated granular flows which are downslope moving inhomogeneous mixtures of sediment, water and air. The deformation and flowing processes characterizing these phenomena are slightly different from the dry granular cases. Whereas solid grain forces dominate the physics of dry granular flows or rock avalanches the solid and fluid forces have to act in concert in cases of fluid-saturated granular flows. Grain friction, grain collision and viscous fluid flow simultaneously transfer momentum. The interaction of solid and fluid forces not only distinguishes fluid-saturated granular flows from dry granular flows but additionally gives them unique destructive power. Like dry granular flows or rock avalanches, debris flows or saturated granular avalanches can occur in real circumstances without or with little warning. The capricious timing and magnitude of such real events hamper collection of detailed data. Scientific understanding has thus been gleaned mostly from qualitative field observations, highly idealized first generation laboratory experiments and theoretical models.

In order to overcome these problems and to reach the goal of reliable predictions of dry and fluid-saturated granular avalanches great efforts have been made to improve the theoretical understanding of these phenomena [3,7,11,12,14–16,23,25,26,33].

In the last decade a model family which is based on the Savage–Hutter theory for shallow dry granular flows has become popular for the description of the time-dependent behaviour of dry granular and fluid-saturated granular flows. Numerous numerical techniques and methods had been developed for the solution of these Savage–Hutter like governing equations for typical moving boundary value problems [1,6–9,13,20,22,27–29,32]. On the one hand these techniques base on a Lagrangian moving mesh finit-difference scheme in which the material is divided into quadrilinear cells (2D) or triangular prisms (3D).

On the other hand there are shock-capturing upwind schemes which are based on approximate Riemann solvers [4,5,10,17,20,32] and very successfully have been applied for gas dynamical and shallow flow problems [20,32,33].

In this context LeVeque [18] developed a new class of wave-propagation methods for the solution of multidimensional hyperbolic systems of conservation laws. These methods are based on the solution of Riemann problems using approximate Riemann solvers for the wave structure and on the introduction of a fluctuation technique which reflects the generalization of the flux difference splitting technique for conservation laws, whereby the left- and the right-going fluctuations reflect the net effect of all left- and all right-going waves. LeVeque et al. [21] extended this class of wave-propagation methods on balance laws operating on spatially varying flux functions. Thereby the source term is used to modify the flux difference before the wave decomposition is performed. This method has great advantages in cases when the classical fractional-step method for the incorporation of more complex source terms fails or produce unrealistic results, because of the two step solving procedure. Thereby, each solving step can be responsible for a little change or imbalance in the solution even though the advection process and the source term representing the net driving force should perfectly cancel out. The changes in the solution are caused by the very different numerical schemes (approximate Riemann solver, ODE-solver) which are applied [20] and responsible for the relatively poor agreement between laboratory and numerical results computed with first order methods concerning the propagation length as function of time and the deposition behaviour in the case of dry and fluid-saturated granular flows [3].

Here I develop a wave-propagation method which operates on the basis of either the Harten, Lax and Van Leer (HLL) or the modified Harten, Lax and Van Leer (HLLC) approximate Riemann solver [10,29] for dry and fluid-saturated shallow granular flows, respectively, for the solution of the Savage–Hutter and the Iverson–Denlinger equations in two dimensions. Comparison between laboratory results [3] and results computed with this new method exhibits good agreement for the propagation length as a function of time, respectively, the propagation velocity, whereas the results computed with the classical fractional-step method reveal significantly lower agreement for the propagation length as a function of time and hence

emphasizes the shortcomings of the fractional-step method in general and especially in the context of free surface flows with more complicated source terms.

Section 2 presents the governing SH- and ID-equations in conservative form for dry and fluid-saturated granular flows.

In Section 3 the new wave-propagation method for dry and fluid-saturated granular flows is developed. It works in the finite volume context with an approximate Riemann solver. Two approximate Riemann solvers, the HLL and the HLLC solver, are used and provide an efficient and elegant possibility, which operates on the basis of an exact Riemann solver, for the location of the front margins and the corresponding velocities.

In Section 4 the method is applied to five laboratory scale problems: (1+2) two dry granular flows down rectangular flumes, (3) a dry granular flow down an inclined plane, (4) a dry granular flow down an inclined plane, whereby the flow is diverted by an obstacle which is located on the inclined plane and (5) a fluid-saturated granular flow down an inclined plane. The inclined rectangular flumes as well as the inclined planes additionally have a smooth transition to a horizontal runout zone, which have different inclination angles. For each experiment the material mixtures are initially hold at rest, start to slide down the flume or the inclined plane after a sudden release, pass the smooth transition zones and come to rest in the horizontal runout zones. Comparison between the results of the numerical and laboratory experiments reveals that the classical fractional-step method computes wrong propagation lengths as function of time, respectively, propagation velocities, whereas the new wave-propagation method computes results which show a good agreement with the laboratory experiments [3]. Section 5 presents the conclusions.

2. Governing equations

Many types of flows can be characterized as shallow-water or shallow flows. The general characteristic of such flows is that all vertical dimensions are much smaller than any typical horizontal scale

$$1 \gg \frac{H}{L}\frac{(\text{vertical length scales})}{(\text{horizontal length scales})}.$$

This allows a considerable simplification in the mathematical formulation by assuming a hydrostatic pressure distribution. However, these flows are not exactly two-dimensional, they exhibit a three-dimensional structure for instance due to bottom topography and bottom friction. In many shallow flows these effects are not essential and it is sufficient to deal with a depth- integrated or depth-averaged form. One popular model family describing the time-dependent behaviour of granular or water saturated granular masses moving down a slope in response to gravitational acceleration (e.g. snow avalanches, landslides, rock falls and debris flows) is based on the Savage–Hutter theory [7,25,26,33]. It assumes an incompressible shallow flow behaviour and that the flowing mass behaves as a Mohr–Coulomb plastic material at yield. The basal shear stress is therefore equal to the normal basal pressure multiplied by a friction coefficient $\tan\phi_{\text{bed}}$, with the basal friction angle ϕ_{bed}. Hereby bed stands for bed level. For water saturated granular masses this SH-theory was partly modified and extended in order to take the interstitial fluid into account, yielding to the ID-equations [3,15,16]. However, this model does not correspond to the SH-theory when the fluid phase vanishes because (1) it does not neglect the cross-slope gradients $\frac{\partial}{\partial y}$ as was done in the SH-theory but (2) it neglects important terms originating from the kinematic bottom boundary condition, taking account of the variable bed slope; these are necessary from physical and mathematical point of views. Here we are dealing with the ID-theory, by taking all the above mentioned terms into account. In conservation-

law form these equations in two-dimensional vector notation are presented below. They describe the flow at time $t \geqslant 0$ at $x, y \in \mathbb{R}$ and read

$$\partial_t \mathbf{q} + \partial_x \mathbf{f}(\mathbf{q}) + \partial_y \mathbf{g}(\mathbf{q}) = \mathbf{S}(\mathbf{q}) \tag{1}$$

with

$$\mathbf{q} := \mathbf{q}(x, y, t) := (h, hu, hv)^{\mathrm{T}}, \tag{2}$$

the flux vectors

$$\mathbf{f}(\mathbf{q}) := \begin{pmatrix} hu \\ hu^2 + \frac{1}{2}[(1-\lambda)k_{\mathrm{a/p}} + \lambda] g_z h^2 \\ \rho uv \end{pmatrix},$$

$$\mathbf{g}(\mathbf{q}) := \begin{pmatrix} \rho v \\ \rho vu \\ \rho v^2 + \frac{1}{2}[(1-\lambda)k_{\mathrm{a/p}} + \lambda] g_z h^2 \end{pmatrix},$$

and the source term vector, representing the net driving force

$$\mathbf{S}(\mathbf{q}) := \begin{pmatrix} 0 \\ -g_z h \frac{\partial z_{\mathrm{bed}}}{\partial x} + s_x \\ -g_z h \frac{\partial z_{\mathrm{bed}}}{\partial y} + s_y \end{pmatrix}.$$

In the expression for $\mathbf{S}(\mathbf{q})$ the first terms represent the above-mentioned contributions omitted by Iverson and Denlinger [16]. The second terms represent the source contributions of the Cauchy stress tensor s_x, s_y and are given by:

$$\begin{aligned} s_x = {} & g_x h - \frac{u}{|\mathbf{v}|}(1-\lambda)\left(g_z + u^2 \frac{\partial \Theta_x}{\partial x}\right) h \tan\phi_{\mathrm{bed}} - \frac{3 v_{\mathrm{f}} \mu}{\rho} \frac{u}{h} + \frac{v_{\mathrm{f}} \mu h}{\rho} \frac{\partial^2 u}{\partial x^2} \\ & - \operatorname{sgn}\left(\frac{\partial u}{\partial y}\right) h k_{\mathrm{a/p}} \cdot \frac{\partial}{\partial y}[g_z h(1-\lambda)] \sin\phi_{\mathrm{int}} + \frac{v_{\mathrm{f}} \mu h}{\rho} \frac{\partial^2 u}{\partial y^2} \end{aligned} \tag{3}$$

and

$$\begin{aligned} s_y = {} & g_y h - \frac{v}{|\mathbf{v}|}(1-\lambda)\left(g_z + v^2 \frac{\partial \Theta_y}{\partial x}\right) h \tan\phi_{\mathrm{bed}} - \frac{3 v_{\mathrm{f}} \mu}{\rho} \frac{v}{h} + \frac{v_{\mathrm{f}} \mu h}{\rho} \frac{\partial^2 v}{\partial x^2} \\ & - \operatorname{sgn}\left(\frac{\partial v}{\partial y}\right) h k_{\mathrm{a/p}} \cdot \frac{\partial}{\partial y}[g_z h(1-\lambda)] \sin\phi_{\mathrm{int}} + \frac{v_{\mathrm{f}} \mu h}{\rho} \frac{\partial^2 v}{\partial y^2}. \end{aligned} \tag{4}$$

Here $k_{\mathrm{a/p}}$ is the earth pressure coefficient, representing the ratio between the normal stress in the down- or cross-slope direction and the vertical normal stress

$$k_{\mathrm{a/p}} = \begin{cases} 2\frac{-\left[1-\cos^2\phi_{\mathrm{int}}(1+\tan^2\phi_{\mathrm{bed}})\right]^{1/2}}{\cos^2\phi_{\mathrm{int}}} - 1 : \left[\left(\frac{\partial u}{\partial x} + \frac{\partial v}{\partial y}\right) < 0\right], \\ 2\frac{+\left[1-\cos^2\phi_{\mathrm{int}}(1+\tan^2\phi_{\mathrm{bed}})\right]^{1/2}}{\cos^2\phi_{\mathrm{int}}} - 1 : \left[\left(\frac{\partial u}{\partial x} + \frac{\partial v}{\partial y}\right) > 0\right]. \end{cases}$$

The subscript a indicates an active stress state corresponding to a dilatation of the material and the subscript p a passive stress state associated with a compression.

The pore pressure $p_{\text{bed}}(x, y, t)$ is described through an advection–diffusion equation

$$\frac{\partial p_{\text{bed}}}{\partial t} + u\frac{\partial p_{\text{bed}}}{\partial x} + v\frac{\partial p_{\text{bed}}}{\partial y} = D\frac{\partial^2 p_{\text{bed}}}{\partial z^2}\bigg|_{\text{bed}}, \tag{5}$$

as proposed by [16]. In this notation h is the flow depth normal to the local bed surface, $\mathbf{v} = (u, v, 0)^{\mathrm{T}}$ the vector of the depth-averaged velocity, $\mathbf{g} = (g_x, g_y, g_z)^{\mathrm{T}}$ the vector of the gravitational acceleration, ϕ_{int}, ϕ_{bed} the internal and the bed friction angle, v_{f} the fluid volume fraction, μ the pore fluid dynamic viscosity, z_{bed} the bottom height function, $\boldsymbol{\Theta} = (\Theta_x, \Theta_y, 0)^{\mathrm{T}}$ the vector of the angle of the local bed slope, $\lambda = \frac{p_{\text{bed}}}{\rho g_z h}$ the ratio between the pore pressure and the normal pressure and D the pore pressure diffusivity.

The system of model Eq. (1) can be rewritten as

$$\partial_t \mathbf{q} + \mathscr{A}\partial_x \mathbf{q} + \mathscr{B}\partial_y \mathbf{q} = \mathbf{S}(\mathbf{q}) \tag{6}$$

with

$$\mathscr{A}(\mathbf{q}) := \frac{\partial \mathbf{q}}{\partial x} = \begin{pmatrix} 0 & 1 & 0 \\ c^2 - u^2 & 2u & 0 \\ -uv & v & u \end{pmatrix}$$

and

$$\mathscr{B}(\mathbf{q}) := \frac{\partial \mathbf{q}}{\partial y} = \begin{pmatrix} 0 & 0 & 1 \\ -uv & v & u \\ c^2 - u^2 & 2u & 0 \end{pmatrix}.$$

The gravity wave speed has the form $c = \sqrt{[(1-\lambda)k_{\text{a/p}} + \lambda]g_z h}$. The eigenvalues of $\mathscr{A}$ and $\mathscr{B}$ are $\lambda_1 = u$, $\lambda_2 = v$, $\lambda_{3/5} = u \pm c$ and $\lambda_{4/6} = v \pm c$. The right and left eigenvector matrices are the same as those for the shallow-water equations but differ in the gravity wave speed [3].

3. Numerical scheme

3.1. Wave-propagation algorithm

The general conservation law in one space dimension

$$\partial_t \mathbf{q} + \partial_x \mathbf{f}(\mathbf{q}) = 0 \tag{7}$$

with $\mathbf{q}(x, t) \in \mathbb{R}^m$ the vector of conserved quantities or the more general variable-coefficient quasi-linear form

$$\partial_t \mathbf{q} + \mathscr{A}(\mathbf{q})\partial_x \mathbf{q} = 0 \tag{8}$$

with $\mathscr{A}(q)$ the Jacobian matrix of $\mathbf{f}$ can be solved on a one-dimensional finite volume grid using a wave-propagation algorithm which bases on the solution of Riemann problems for the wave structure and the introduction of a fluctuation splitting technique and was developed by LeVeque [18].

The approximate solution of the Riemann problem consisting of Eq. (7) and the initial data

$$\mathbf{q}(x, t = 0) = \begin{cases} \mathbf{q}_l & (x < 0), \\ \mathbf{q}_r & (x > 0) \end{cases}$$

is derived using Eq. (8). This requires the approximation of cell averages over the ith time interval $\Delta t_n = t_{n+1} - t_n$

$$\mathbf{Q}_i \approx \frac{1}{\Delta x}\int_{x_{i-\frac{1}{2}}}^{x_{i+\frac{1}{2}}} \mathbf{q}(x,t_n)\,\mathrm{d}x \tag{9}$$

with $\Delta x = x_{i+\frac{1}{2}} - x_{i-\frac{1}{2}}$ and the definition of an approximate Jacobian matrix $\mathscr{A}_{i-\frac{1}{2}}$ at the interface $x_{i-\frac{1}{2}}$ between two cells $C_i = [x_{i-\frac{1}{2}}, x_{i+\frac{1}{2}}]$ and $C_{i-1} = [x_{i-\frac{3}{2}}, x_{i-\frac{1}{2}}]$ which reflects the wave structure at the interface.

The solution of the one-dimensional Riemann problem between the cells i and $i-1$, $\mathscr{C}_i$, $\mathscr{C}_{i-1}$ can then be expressed as a set of waves

$$\mathbf{Q}_i - \mathbf{Q}_{i-1} = \sum_{p=1}^{m} \alpha^p_{i-\frac{1}{2}}\mathbf{r}^p_{i-\frac{1}{2}} = \sum_{p=1}^{m} \mathscr{W}^p_{i-\frac{1}{2}} \tag{10}$$

with $\alpha^p_{i-\frac{1}{2}}$ the wave strength of the pth wave and the eigenvector $\mathbf{r}^p_{i-\frac{1}{2}}$. Each wave changes the cell averages by a certain amount with the consequence that the averages at time $t+\Delta t$ can be found by simply adding these independent amounts. Here $\mathscr{W}^m \in \mathbb{R}^m$ is the jump across the mth wave with an associated wave speed $s^m \in \mathbb{R}$.

The net effect of all left-going and all right-going waves on the cell averages are represented by the symbols $\mathscr{A}^+\Delta\mathbf{Q}_{i-\frac{1}{2}}$ and $\mathscr{A}^-\Delta\mathbf{Q}_{i-\frac{1}{2}}$. They should be interpreted as single functional entities that are measures for the net effect of all right- and all left-going waves, originating at point $x_{i-\frac{1}{2}}$ and are called fluctuations. Note that within the cell $\mathscr{C}_i$ the right-going fluctuations from the left edge $\mathscr{A}^+\Delta\mathbf{Q}_{i-\frac{1}{2}}$ and the left-going fluctuations from the right edge $\mathscr{A}^-\Delta\mathbf{Q}_{i+\frac{1}{2}}$ affect the cell averages as shown in Fig. 1. The fluctuations $\mathscr{A}^+\Delta\mathbf{Q}_{i-\frac{1}{2}}$ and $\mathscr{A}^-\Delta\mathbf{Q}_{i-\frac{1}{2}}$ are motivated through the assumption of a constant coefficient linear system

$$\partial_t\mathbf{q} + \mathscr{A}\partial_x\mathbf{q} = 0. \tag{11}$$

The fluctuation matrices are $\mathscr{A}^\pm = \mathscr{R}\Lambda^\pm\mathscr{R}^{-1}$ with $\mathscr{A}_{i-\frac{1}{2}} = \mathscr{A}^+ + \mathscr{A}^-$, $\mathscr{R} = [\mathbf{r}^1|\mathbf{r}^2\cdot|\mathbf{r}^m]$ the matrix of right eigenvectors and $\Lambda = \mathrm{diag}(s^1, s^2, \ldots, s^m)$ the eigenvalue matrix of the Jacobian and $\Lambda^\pm = \mathrm{diag}((s^1)^\pm, (s^2)^\pm, \ldots, (s^m)^\pm)$.

The Godunov method in the wave-propagation form is now given by

$$\mathbf{Q}_i^{n+1} = \mathbf{Q}_i^n - \frac{\Delta t}{\Delta x}\left[\mathscr{A}^+\Delta\mathbf{Q}_{i-\frac{1}{2}} + \mathscr{A}^-\Delta\mathbf{Q}_{i+\frac{1}{2}}\right]. \tag{12}$$

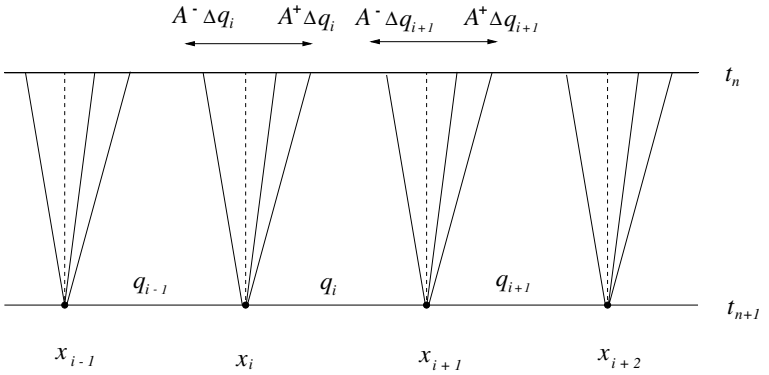

Fig. 1. Waves and fluctuations for the one-dimensional Godunov method.

For a given set of data $\mathbf{Q}_{i-1}$, $\mathbf{Q}_i$, an appropriate Riemann solution should define functions $\hat{\mathbf{Q}}^{m-1}_{i-\frac{1}{2}}(\frac{x}{t})$ that approximate the true solution of the intermediate states arising through the process of connecting $\mathbf{Q}_{i-1}$, $\mathbf{Q}_i$ by a sequence of discontinuities.

If the approximate Riemann solver is conservative it has to satisfy the following property:

$$\mathscr{A}^+\Delta\mathbf{Q}_{i-\frac{1}{2}} + \mathscr{A}^-\Delta\mathbf{Q}_{i-\frac{1}{2}} = \mathbf{f}(\mathbf{Q}_i) - \mathbf{f}(\mathbf{Q}_{i-1}). \tag{13}$$

The fluctuations of the Godunov method at the interface $x_{i-\frac{1}{2}}$ are

$$\begin{aligned}
\mathscr{A}^+\Delta\mathbf{Q}_{i-\frac{1}{2}} &= \mathbf{f}\left(\hat{\mathbf{Q}}^{m-1}_{i-\frac{1}{2}}\right) - \mathbf{f}(\mathbf{Q}_{i-1}) \doteq \sum_{p=1}^{m} (s^p_{i-\frac{1}{2}})^+ \mathscr{W}^p_{i-\frac{1}{2}},\\
\mathscr{A}^-\Delta\mathbf{Q}_{i-\frac{1}{2}} &= \mathbf{f}(\mathbf{Q}_i) - \mathbf{f}(\hat{\mathbf{Q}}^{m-1}_{i-\frac{1}{2}}) \doteq \sum_{p=1}^{m} (s^p_{i-\frac{1}{2}})^- \mathscr{W}^p_{i-\frac{1}{2}}
\end{aligned} \tag{14}$$

with $(s^p_{i-\frac{1}{2}})^+$ and $(s^p_{i-\frac{1}{2}})^-$ the wave speeds with positive and negative signs, respectively. The Godunov method in the wave-propagation form may adequately be presented as

$$\mathbf{Q}^{n+1}_i = \mathbf{Q}^n_i - \frac{\Delta t}{\Delta x}\left[\sum_{p=1}^{m} (s^p_{i-\frac{1}{2}})^+ \mathscr{W}^p_{i-\frac{1}{2}} + \sum_{p=1}^{m} (s^p_{i+\frac{1}{2}})^- \mathscr{W}^p_{i+\frac{1}{2}}\right]. \tag{15}$$

This algorithm can be extended to a high-resolution version

$$\begin{aligned}
\mathbf{Q}^{n+1}_i = \mathbf{Q}^n_i &- \frac{\Delta t}{\Delta x}\left[\sum_{p=1}^{m} (s^p_{i-\frac{1}{2}})^+ \mathscr{W}^p_{i-\frac{1}{2}} + \sum_{p=1}^{m} (s^p_{i+\frac{1}{2}})^- \mathscr{W}^p_{i+\frac{1}{2}}\right]\\
&+ \frac{\Delta t^2}{\Delta 2x^2}\left[\sum_{p=1}^{m}\left((s^p_{i-\frac{1}{2}})^+\right)^2 \mathscr{W}^p_{i-\frac{1}{2}} - \sum_{p=1}^{m}\left((s^p_{i+\frac{1}{2}})^-\right)^2 \mathscr{W}^p_{i+\frac{1}{2}}\right]
\end{aligned} \tag{16}$$

as presented by [19].

With a source term $\mathbf{S}(\mathbf{q})$ the balance law

$$\partial_t\mathbf{q} + \partial_x\mathbf{f}(\mathbf{q}) = \mathbf{S}(\mathbf{q}) \tag{17}$$

replaces the conservation law. The solution requires an extension of the algorithm, which effectively involves the determination of the Jacobian $\mathscr{A}_{i-\frac{1}{2}}$ at the interface $x_{i-\frac{1}{2}}$ or in other words the decomposition of the difference between the flux difference and the source term

$$\mathscr{A}_{i-\frac{1}{2}}(\mathbf{Q}_i - \mathbf{Q}_{i-1}) = \mathbf{f}_i(\mathbf{Q}_i) - \mathbf{f}_{i-1}(\mathbf{Q}_{i-1}) - \Delta x\mathbf{S}_{i-\frac{1}{2}} \tag{18}$$

into waves [21].

The fluctuation equation (14) is modified as follows:

$$\begin{aligned}
\mathscr{A}^+\Delta\mathbf{Q}_{i-\frac{1}{2}} &= \mathbf{f}\left(\hat{\mathbf{Q}}^{m-1}_{i-\frac{1}{2}}\right) - \mathbf{f}(\mathbf{Q}_{i-1}) - \Delta x\mathbf{S}_{i-\frac{1}{2}} \doteq \sum_{p=1}^{m} (s^p_{i-\frac{1}{2}})^+ \mathscr{W}^p_{i-\frac{1}{2}} - \Delta x\mathbf{S}_{i-\frac{1}{2}},\\
\mathscr{A}^-\Delta\mathbf{Q}_{i-\frac{1}{2}} &= \mathbf{f}(\mathbf{Q}_i) - \mathbf{f}(\hat{\mathbf{Q}}^{m-1}_{i-\frac{1}{2}}) \doteq \sum_{p=1}^{m} (s^p_{i-\frac{1}{2}})^- \mathscr{W}^p_{i-\frac{1}{2}} - \Delta x\mathbf{S}_{i-\frac{1}{2}}.
\end{aligned} \tag{19}$$

The generated waves carry no increments in the conservative variables $\mathbf{q}$ but flux increments. They have the form of $\mathbf{q}$-increments multiplied by the wave speed. Each wave changes the fluctuations by a certain amount

with the consequence that resulting fluctuations for left- and right-going waves can be found by simply adding up these independent contributions. The relation between the standard wave-propagation algorithm (Section 3.1) and the modified wave-propagation algorithm taking a source term into account lies in the relevance of conditions (13) and (18), which represent the Rankine–Hugoniot relation with $s = 0$ [21].

The higher order Godunov method in the wave-propagation form that accounts for a source term is

$$\begin{aligned}\mathbf{Q}_i^{n+1} = \mathbf{Q}_i^n &- \frac{\Delta t}{\Delta x}\left[\sum_{p=1}^{m}(s^p_{i-\frac{1}{2}})^+ \mathscr{W}^p_{i-\frac{1}{2}} - \Delta x \mathbf{S}_{i+\frac{1}{2}} + \sum_{p=1}^{m}(s^p_{i+\frac{1}{2}})^- \mathscr{W}^p_{i+\frac{1}{2}} - \Delta x \mathbf{S}_{i+\frac{1}{2}}\right] \\ &+ \frac{\Delta t^2}{2\Delta x^2}\left[\sum_{p=1}^{m}\left((s^p_{i-\frac{1}{2}})^+\right)^2 \mathscr{W}^p_{i-\frac{1}{2}} - \Delta x \mathbf{S}_{i-\frac{1}{2}} - \sum_{p=1}^{m}\left((s^p_{i+\frac{1}{2}})^-\right)^2 \mathscr{W}^p_{i+\frac{1}{2}} - \Delta x \mathbf{S}_{i+\frac{1}{2}}\right] \\ &- \frac{\Delta t^2}{2\Delta x^2}\left[\mathbf{S}_q(\mathbf{Q}_i)\sum_{p=1}^{m}\frac{1}{2}\left((s^p_{i-\frac{1}{2}})^+ \mathscr{W}^p_{i-\frac{1}{2}} - \Delta x \mathbf{S}_{i-\frac{1}{2}} + (s^p_{i+\frac{1}{2}})^- \mathscr{W}^p_{i+\frac{1}{2}} - \Delta x \mathbf{S}_{i+\frac{1}{2}}\right)\right]\end{aligned} \tag{20}$$

with $\mathbf{S}_q(\mathbf{Q}_i)$ the Jacobian of the discretized source term vector.

3.2. The HLL approximate Riemann solver

Considering given states $\mathbf{Q}_{i-1}$, $\mathbf{Q}_i$ the solution of the Riemann problem will yield a set of waves at the interface $x_{i-\frac{1}{2}}$. The HLL approximate Riemann solver is based on the estimate of the smallest and the largest wave speeds arising in the Riemann solution [32]. There are two waves $\mathscr{W}^1_{i-\frac{1}{2}}$, $\mathscr{W}^2_{i-\frac{1}{2}}$ with corresponding speeds $s^1_{i-\frac{1}{2}}$, $s^2_{i-\frac{1}{2}}$ and one intermediate state $\hat{\mathbf{Q}}^1_{i-\frac{1}{2}}$. It is determined through the assumption that the approximate solution satisfies Eq. (13)

$$\mathbf{f}(\mathbf{Q}_i) - \mathbf{f}(\mathbf{Q}_{i-1}) = s^1_{i-\frac{1}{2}}(\hat{\mathbf{Q}}^1_{i-\frac{1}{2}} - \mathbf{Q}_{i-1}) + s^2_{i-\frac{1}{2}}\left(\mathbf{Q}_i - \hat{\mathbf{Q}}^1_{i-\frac{1}{2}}\right). \tag{21}$$

After some algebra it follows for $\hat{\mathbf{Q}}^1_{i-\frac{1}{2}}$:

$$\hat{\mathbf{Q}}^1_{i-\frac{1}{2}} = \frac{\mathbf{f}(\mathbf{Q}_i) - \mathbf{f}(\mathbf{Q}_{i-1}) - s^2_{i-\frac{1}{2}}\mathbf{Q}_i + s^1_{i-\frac{1}{2}}\mathbf{Q}_{i-1}}{s^1_{i-\frac{1}{2}} - s^2_{i-\frac{1}{2}}}. \tag{22}$$

The waves have the form

$$\mathscr{W}^1_{i-\frac{1}{2}} = \hat{\mathbf{Q}}^1_{i-\frac{1}{2}} - \mathbf{Q}_{i-1}, \quad \mathscr{W}^2_{i-\frac{1}{2}} = \mathbf{Q}_i - \hat{\mathbf{Q}}^1_{i-\frac{1}{2}}$$

and the wave speeds $s^1_{i-\frac{1}{2}}$, $s^2_{i-\frac{1}{2}}$ are estimated through the left and right eigenvalues

$$s^1_{i-\frac{1}{2}} = u_{i-1} - \sqrt{gh_{i-1}}, \quad s^2_{i-\frac{1}{2}} = u_i + \sqrt{gh_i}$$

with h_i, u_i the flow height and depth-averaged horizontal velocity and g the gravitational acceleration. Taking a source term into account changes the fluctuation equation (19) for the HLL-solver ($m = 2$) to

$$\begin{aligned}\mathscr{A}^+\Delta\mathbf{Q}_{i-\frac{1}{2}} &= \sum_{p=1}^{2}(s^p_{i-\frac{1}{2}})^+ \mathscr{W}^p_{i-\frac{1}{2}} - \Delta x \mathbf{S}_{i-\frac{1}{2}}, \\ \mathscr{A}^-\Delta\mathbf{Q}_{i-\frac{1}{2}} &= \sum_{p=1}^{2}(s^p_{i-\frac{1}{2}})^- \mathscr{W}^p_{i-\frac{1}{2}} - \Delta x \mathbf{S}_{i-\frac{1}{2}},\end{aligned} \tag{23}$$

which has to be substituted in Eq. (15).

3.3. The HLLC approximate Riemann solver

The HLLC approximate Riemann solver is an improved version of the HLL solver (Section 3.2) since it contains an additional wave, the so-called contact discontinuity [29]. Considering the same Riemann problem as for the HLL case three waves will be generated at the interface $x_{i-\frac{1}{2}}$ with two intermediate states, $\hat{\mathbf{Q}}^1_{i-\frac{1}{2}}$ and $\hat{\mathbf{Q}}^2_{i-\frac{1}{2}}$. The assumption is made that the wave speed estimates $s^p_{i-\frac{1}{2}}$ for $p = 1, 2, 3$ are available with $s^1_{i-\frac{1}{2}} < s^2_{i-\frac{1}{2}} < s^3_{i-\frac{1}{2}}$ and that the speeds $s^1_{i-\frac{1}{2}}$, $s^3_{i-\frac{1}{2}}$ correspond to the two waves of the HLL-solver and are estimated by

$$s^1_{i-\frac{1}{2}} = u_{i-1} - \sqrt{gh_{i-1}}, \quad s^3_{i-\frac{1}{2}} = u_i + \sqrt{gh_i}.$$

If the flow heights h_i, h_{i-1} do not vanish, the speed of the additional wave $s^2_{i-\frac{1}{2}}$ is assumed to be the speed of the intermediate state of an approximate Riemann solver dealing with two rarefactions, having the form $s^2_{i-\frac{1}{2}} = \frac{1}{2}(u_i + u_{i-1}) - \sqrt{gh_i} + \sqrt{gh_{i-1}}$. Here u_i, u_{i-1} are the depth-averaged horizontal velocities in the cells $\mathscr{C}_i$, $\mathscr{C}_{i-1}$. If either $h_i = 0$, $h_{i-1} \neq 0$ or $h_i \neq 0$, $h_{i-1} = 0$ hold, the speed $s^2_{i-\frac{1}{2}}$ of the additional wave is

$$s^2_{i-\frac{1}{2}} = \frac{s^1_{i-\frac{1}{2}} h_i (u_i - s^3_{i-\frac{1}{2}}) - s^3_{i-\frac{1}{2}} h_{i-1}(u_{i-1} - s^1_{i-\frac{1}{2}})}{h_i(u_i - s^3_{i-\frac{1}{2}}) - h_{i-1}(u_{i-1} - s^1_{i-\frac{1}{2}})}. \tag{24}$$

This form for the speed $s^2_{i-\frac{1}{2}}$ and the intermediate states are determined by assuming that the approximate solutions must satisfy condition (13) as for the HLL-solver in Section 3.2

$$\begin{aligned} &\mathbf{f}(\hat{\mathbf{Q}}^1_{i-\frac{1}{2}}) - \mathbf{f}(\mathbf{Q}_{i-1}) = s^1_{i-\frac{1}{2}}(\hat{\mathbf{Q}}^1_{i-\frac{1}{2}} - \mathbf{Q}_{i-1}), \\ &\mathbf{f}(\mathbf{Q}_i) - \mathbf{f}(\hat{\mathbf{Q}}^2_{i-\frac{1}{2}}) = s^3_{i-\frac{1}{2}}(\mathbf{Q}_i - \hat{\mathbf{Q}}^2_{i-\frac{1}{2}}), \end{aligned} \tag{25}$$

which leads to the following expressions for the intermediate states

$$\hat{\mathbf{Q}}^1_{i-\frac{1}{2}} = \frac{\mathbf{f}(\hat{\mathbf{Q}}^1_{i-\frac{1}{2}}) - \mathbf{f}(\mathbf{Q}_{i-1})}{s^1_{i-\frac{1}{2}}} + \mathbf{Q}_{i-1}, \quad \hat{\mathbf{Q}}^2_{i-\frac{1}{2}} = \frac{\mathbf{f}(\hat{\mathbf{Q}}^2_{i-\frac{1}{2}}) - \mathbf{f}(\mathbf{Q}_i)}{s^3_{i-\frac{1}{2}}} + \mathbf{Q}_i$$

or in vector representation

$$\hat{\mathbf{Q}}^1_{i-\frac{1}{2}} = \frac{h_{i-1}(s^1_{i-\frac{1}{2}} - u_{i-1})}{s^1_{i-\frac{1}{2}} - s^2_{i-\frac{1}{2}}} \cdot \begin{bmatrix} 1 \\ s^2_{i-\frac{1}{2}} \end{bmatrix}, \quad \hat{\mathbf{Q}}^2_{i-\frac{1}{2}} = \frac{h_i(s^3_{i-\frac{1}{2}} - u_i)}{s^3_{i-\frac{1}{2}} - s^2_{i-\frac{1}{2}}} \cdot \begin{bmatrix} 1 \\ s^2_{i-\frac{1}{2}} \end{bmatrix}.$$

The corresponding waves have the form

$$\mathscr{W}^1_{i-\frac{1}{2}} = \hat{\mathbf{Q}}^1_{i-\frac{1}{2}} - \mathbf{Q}_{i-1}, \quad \mathscr{W}^2_{i-\frac{1}{2}} = \hat{\mathbf{Q}}^2_{i-\frac{1}{2}} - \hat{\mathbf{Q}}^1_{i-\frac{1}{2}}, \quad \mathscr{W}^3_{i-\frac{1}{2}} = \mathbf{Q}_i - \hat{\mathbf{Q}}^2_{i-\frac{1}{2}}. \tag{26}$$

Considering the first components of the vector equations (25) and taking into account that $h_i = h_{i-1}$ for an exact Riemann solver, Eq. (24), for the speed of wave $s^2_{i-\frac{1}{2}}$ follows after some algebra.

The fluctuations (14) for the HLLC-solver ($m = 3$) have to be modified in case of a source term, yielding the form

$$\begin{aligned}\mathscr{A}^{+}\Delta\mathbf{Q}_{i-\frac{1}{2}} &= \sum_{p=1}^{3}\left(s^{p}_{i-\frac{1}{2}}\right)^{+}\mathscr{W}^{p}_{i-\frac{1}{2}} - \Delta x\mathbf{S}_{i-\frac{1}{2}},\\ \mathscr{A}^{-}\Delta\mathbf{Q}_{i-\frac{1}{2}} &= \sum_{p=1}^{3}\left(s^{p}_{i-\frac{1}{2}}\right)^{-}\mathscr{W}^{p}_{i-\frac{1}{2}} - \Delta x\mathbf{S}_{i-\frac{1}{2}}.\end{aligned} \tag{27}$$

3.4. Approximate Riemann solver for a dry bed

In many applications (e.g. moving water fronts, damm break problems, avalanches, debris flows, etc.) the downslope moving material has a finite extension and is confined by a boundary which moves with the flow velocity. Outside this boundary is a vacuum, which means that there is a wet region adjacent to a dry region. The exact determination of wet/dry front velocities is essential and justifies the application of the shock-capturing approach involving the utilization of a single scheme for the complete domain. Shock-waves as well as rarefaction waves emerge as part of the solution and are easily extractable in special cases like wet/dry fronts. Basically the governing equation (1) represents a continuum description and do not hold in dry regions. In the numerical computation of shallow flows, there are only minor problems in cases with flow heights $h > 0$ everywhere, whereas in regions with $h = 0$ adjacent to regions with $h > 0$ serious computational problems might occur, because the velocity in the dry regions is not well defined. The equations have to be solved in the wet region right up to the boundary between both regions. The simplest case is the horizontal dam adjacent to a dry horizontal region, representing the general form for the one-dimensional Riemann problem (7), with the initial data

$$q(x, t=0) = \begin{cases} q_{\text{wet}} & (x < 0),\\ q_{\text{dry}} & (x > 0).\end{cases}$$

Fig. 2 shows the solutions of the one-dimensional wet/dry Riemann problem with the dry bed initial data on the right side (upper) and on the left side (lower), respectively. For a dry bed on the right side the solution consists of a single left rarefaction which speed is associated with the left eigenvalue $s^{1}_{i-\frac{1}{2}} = u_{i-1} - \sqrt{gh_{i-1}}$. There is no shock because a shock wave cannot be adjacent to a dry region. The wet/dry front corresponds to the tail of the left rarefaction and has the exact propagation speed $s^{1}_{i-\frac{1}{2}}$. For a dry bed on the left side the solution consists of a single right rarefaction wave, whereby the speed is associated with the right eigenvalue $s^{2}_{i-\frac{1}{2}} = u_i + \sqrt{gh_i}$. In the second case the wet/dry front corresponds to the tail of the right rarefaction and has the exact propagation speed $s^{2}_{i-\frac{1}{2}}$ [32].

The HLL and the HLLC approximate Riemann solvers offer a simple way of dealing with dry bed situations and the determination of the wet/dry front velocities [30]. The required wave speed estimates are $s^{1}_{i-\frac{1}{2}}$, $s^{2}_{i-\frac{1}{2}}$ for the HLL-solver and $s^{1}_{i-\frac{1}{2}}$, $s^{2}_{i-\frac{1}{2}}$ and $s^{3}_{i-\frac{1}{2}}$ for the HLLC-solver. For the HLL-solver the wave speeds are estimated as the exact dry front speeds through

$$s^{1}_{i-\frac{1}{2}} = \begin{cases} u_i - 2\sqrt{gh_i} & \text{if } (h_{i-1} = 0,\ h_i > 0),\\ u_{i-1} - \sqrt{gh_{i-1}} & \text{if } (h_{i-1} > 0,\ h_i = 0),\end{cases}$$

$$s^{2}_{i-\frac{1}{2}} = \begin{cases} u_{i-1} + 2\sqrt{gh_{i-1}} & \text{if } (h_{i-1} > 0,\ h_i = 0),\\ u_i + \sqrt{gh_i} & \text{if } (h_{i-1} = 0,\ h_i > 0),\end{cases}$$

whereas the wave speeds for the HLLC-solver have the following form taking the contact discontinuity $s^{2}_{i-\frac{1}{2}}$ into account

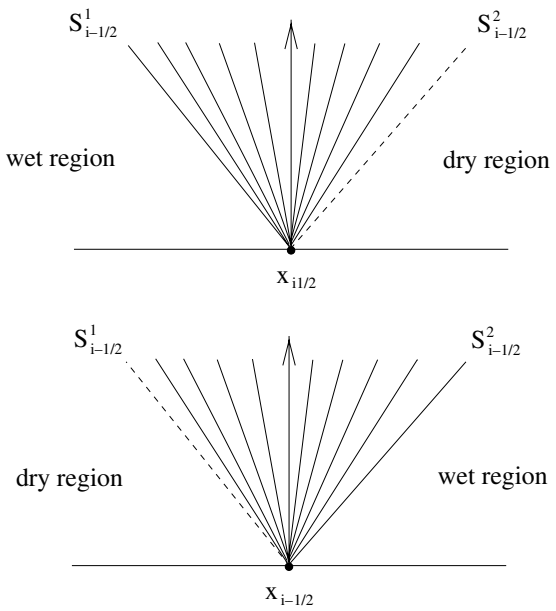

Fig. 2. Solution of the Riemann problem involving a dry bed state. Upper: For the dry bed on the right side the solution consists of a single left rarefaction wave. Lower: For the dry state on the left side the solution consists of a single right rarefaction wave.

$$s^1_{i-\frac{1}{2}} = \begin{cases} u_i - 2\sqrt{gh_i} & \text{if } (h_{i-1} = 0,\ h_i > 0), \\ u_{i-1} - \sqrt{gh_{i-1}} & \text{if } (h_{i-1} > 0,\ h_i = 0), \end{cases}$$

$$s^2_{i-\frac{1}{2}} = \begin{cases} \dfrac{s^1_{i-\frac{1}{2}} h_i (u_i - s^3_{i-\frac{1}{2}}) - s^3_{i-\frac{1}{2}} h_{i-1} (u_{i-1} - s^1_{i-\frac{1}{2}})}{h_i (u_i - s^3_{i-\frac{1}{2}}) - h_{i-1} (u_{i-1} - s^1_{i-\frac{1}{2}})} & \text{if } (h_{i-1} = 0 \text{ or } h_i = 0), \\ \frac{1}{2}(u_i + u_{i-1}) + \sqrt{gh_i} + \sqrt{gh_{i-1}} & \text{if } (h_{i-1} > 0,\ h_i > 0), \end{cases}$$

$$s^3_{i-\frac{1}{2}} = \begin{cases} u_{i-1} + 2\sqrt{gh_{i-1}} & \text{if } (h_{i-1} > 0,\ h_i = 0), \\ u_i + \sqrt{gh_i} & \text{if } (h_{i-1} = 0,\ h_i > 0). \end{cases}$$

4. Numerical experiments

Since our focus lies on the application of the first order and not of the second order method, the first one consisting of the HLLC approximate Riemann solver (Sections 3.3 and 3.4) and the wave-propagation approach (Section 3.1) in the balance law context is applied to the following test problems.

Problem I: A dry granular mixture with a total volume of 290 cm^3 downslides an inclined rectangular flume. The experimental conditions are the same as in a laboratory experiment carried out by [3] which serves as a reference solution. The inclination angle $\boldsymbol{\Theta}(x, y)$ and the experimental setup will be determined in Section 4.1.

Problem II: 1500 cm^3 of the dry mixture downslides the rectangular flume having a different inclination angle as in the first test problem (to be determined in Section 4.1). In this experiment the ability of the numerical scheme to handle travelling shock waves is investigated [7,27,28,33].

Problem III: The dry mixture with a total volume of 290 cm^3 downslides an inclined plane having the same inclination angle as in test problem I.

Problem IV: 800 cm^3 of the dry mixture downslides the inclined plane which has the same inclinations angle as in test problem II. The flow is diverted by an obstacle located on the inclined plane.

Problem V: A fluid-saturated granular mixture with a total volume of 290 cm^3 downslides the same inclined plane as in test problem III.

These computational experiments serve as realistic testcases concerning the incorporation of complicated source terms using the wave-propagation approach (Section 3.1) with the HLLC Riemann solver. Since there is only in the case of test problem I a reference solution the results of the other computational experiments are judged through the results computed with the first order method in the fractional-step context [21]. In so doing the solution and integration of system (1) using the fractional-step approach involves a two-step solving procedure. In the first step only the homogeneous part of the system is solved with the HLLC approximate Riemann solver (Sections 3.3 and 3.4), assuming that the source term vector is identically zero ($\mathbf{S}(\mathbf{q}) = 0$). In the second step the real source term is taken into account and requires the integration of the ordinary differential equation

$$\frac{d\mathbf{q}}{dt} = \mathbf{S}(\mathbf{q}) \tag{28}$$

in the time interval Δt, with the solution of the homogeneous part as the initial condition. The solution of the ODE is achieved by using an explicit Euler method, which delivers first order accuracy in space and time [31].

4.1. Rectangular-flume experiments (I, II)

The computational domain in the experiments I and II is a rectangle with$x \in [0, 2.2] \times y \in [-0.1, 0.1]$. It consists of an inclined region, a horizontal runout and a smooth transition region in between. The regions are characterized by the inclination angle $\boldsymbol{\Theta}(x, y) = (\Theta_x, 0, 0)^{\mathrm{T}}$. In the case of experiment I it has the form

$$\Theta_x(x) = \begin{cases} \Theta_0 : & (x \leqslant 1.0), \\ \Theta_0(1 - (x - 1.0)/0.05) : & (1.0 < x < 1.05), \\ 0 : & (x \geqslant 1.05) \end{cases}$$

with $\Theta_0 = 31.4°$.

Table 1
Material properties essential for the numerical simulation of the dry and the fluid-saturated granular flow experiments

Parameter	Dry granular flow	Fluid-saturated granular flow
Basal friction angle ϕ_{bed} (°)	29	28
Internal friction angle ϕ_{int} (°)	40	42
Solid volume fraction v_{s}	0.6	0.6
Fluid volume fraction v_{f}	0.4	0.4
Fluid viscosity μ (Pa s)	2×10^{-5} (air)	0.1 (muddy water)
Solid density ρ_{s} (kg/m)	2650 (quartz)	2700 (quartz, feldspar, etc.)
Fluid density ρ_{f} (kg/m)	1 (air)	1200 (muddy water)
Mixture bulk density ρ (kg/m)	1600	2000
Hydraulic diffusivity D (m/s^2)	0.05	10^{-4}
Initial pore pressure ratio	0.0	0.9

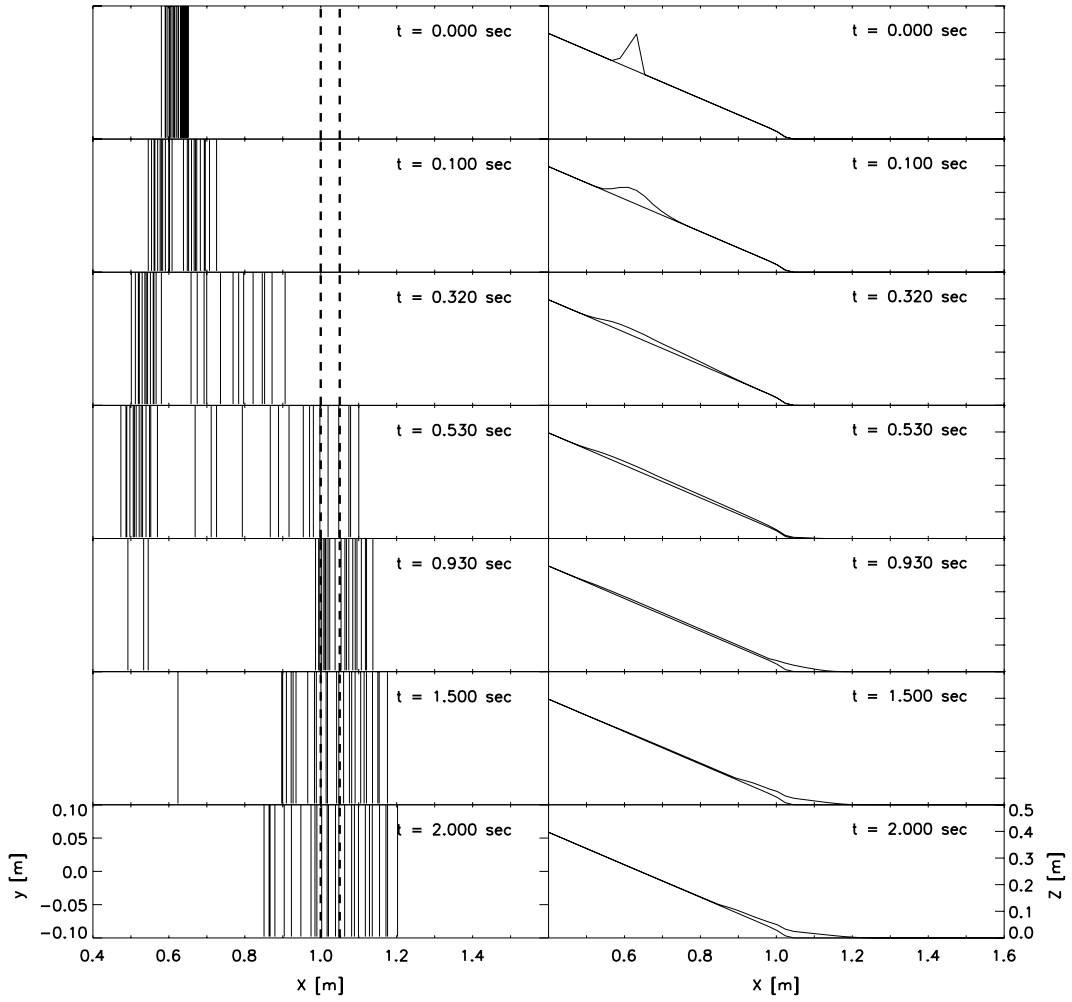

Fig. 3. Dry granular mixture flow height of the rectangular-flume experiment computed with the wave-propagation method. The rectangular flume consists of an inclined region ($x < 1.0$) with inclination angle $\Theta_0 = 31.4°$, a horizontal runout ($x > 1.05$) and a smooth transition region in between ($1.0 < x < 1.05$). Left: Isoline representation of the flow height as function of time. Contours depict 1-mm isopachs of flow thickness normal to the bed. Right: Vertical slice (x–z) of the flow height on the bed surface, multiplied by a factor of 3 for a better visualization.

The initial condition for the flow height $h(x, y)$ of the dry granular material is

$$h(x) = \begin{cases} 0.879897 \sin(\pi(x - 0.58)) - 0.3 \sin(2\pi(x - 0.58)) : & x \in [0.58, 0.635], \\ 0 : & \text{else.} \end{cases}$$

In the case of experiment II the inclination angle $\boldsymbol{\Theta}(x, y)$ and the initial condition for the flow height $h(x, y)$ are

$$\Theta_x(x) = \begin{cases} \Theta_0 : & (x \leqslant 0.8), \\ \Theta_0(1 - (x - 0.8)/0.15) : & (0.8 < x < 0.95), \\ 0 : & (x \geqslant 0.95) \end{cases}$$

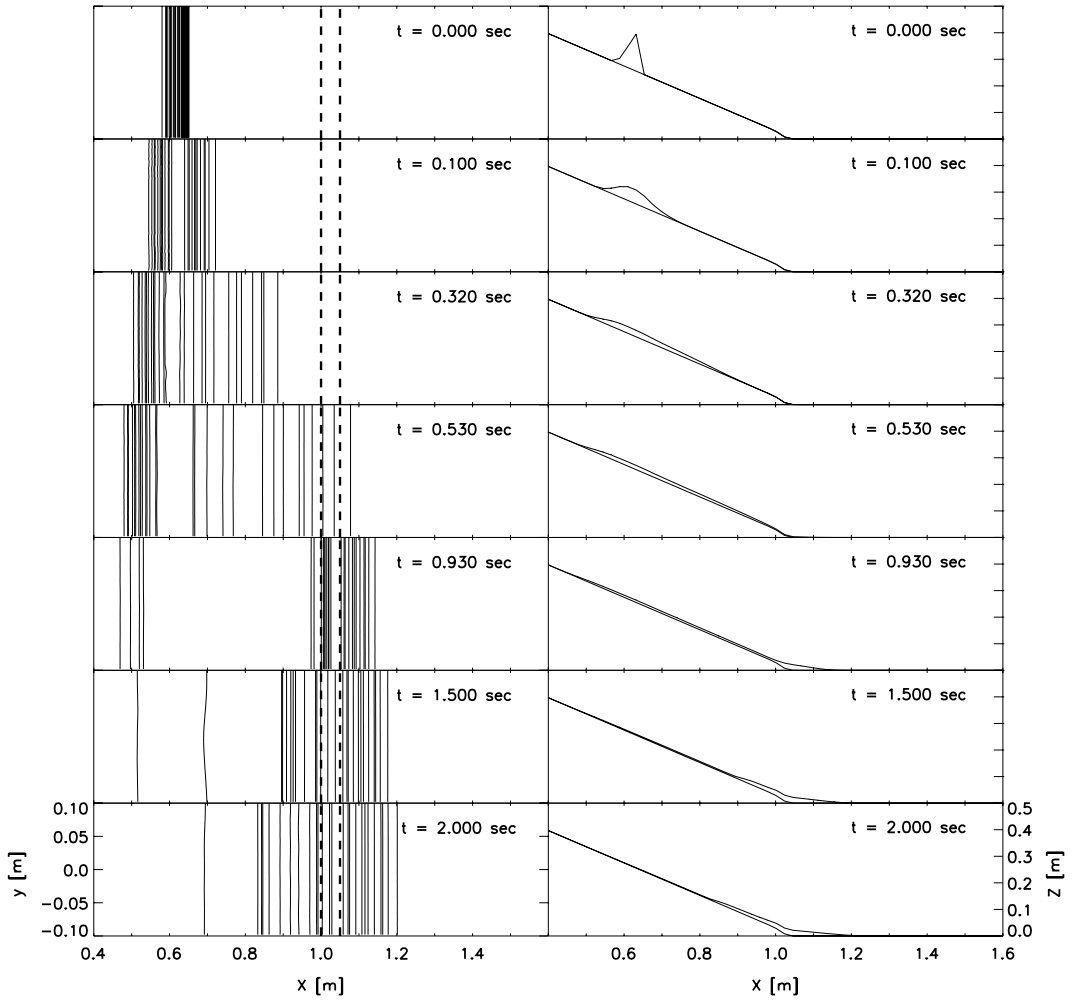

Fig. 4. Dry granular mixture flow height of the rectangular-flume experiment computed with the fractional-step method. The rectangular flume consists of an inclined region ($x < 1.0$) with inclination angle $\Theta_0 = 31.4°$, a horizontal runout ($x > 1.05$) and a smooth transition region in between ($1.0 < x < 1.05$). Left: Isoline representation of the flow height as function of time. Contours depict 1-mm isopachs of flow thickness normal to the bed. Right: Vertical slice (x–z) of the flow height on the bed surface, multiplied by a factor of 3 for a better visualization.

with $\Theta_0 = 40°$ and

$$h(x) = \begin{cases} 5(0.879897\sin(\pi(x-0.58)) - 0.3\sin(2\pi(x-0.58))) : & x \in [0.58, 0.635], \\ 0 : & \text{else.} \end{cases}$$

4.2. Inclined plane experiments (III–V)

The computational domain in the inclined plane experiments has the dimensions $x \in [0, 2.2] \times y \in [-0.3, 0.3]$. As in the experiments I and II it consists of an inclined region, a horizontal runout and a smooth transition region in between. In the cases of the experiments III and V the inclination angle $\boldsymbol{\Theta}(x, y)$ has the same form as in experiment I. The initial conditions for the flow height of the dry and the saturated

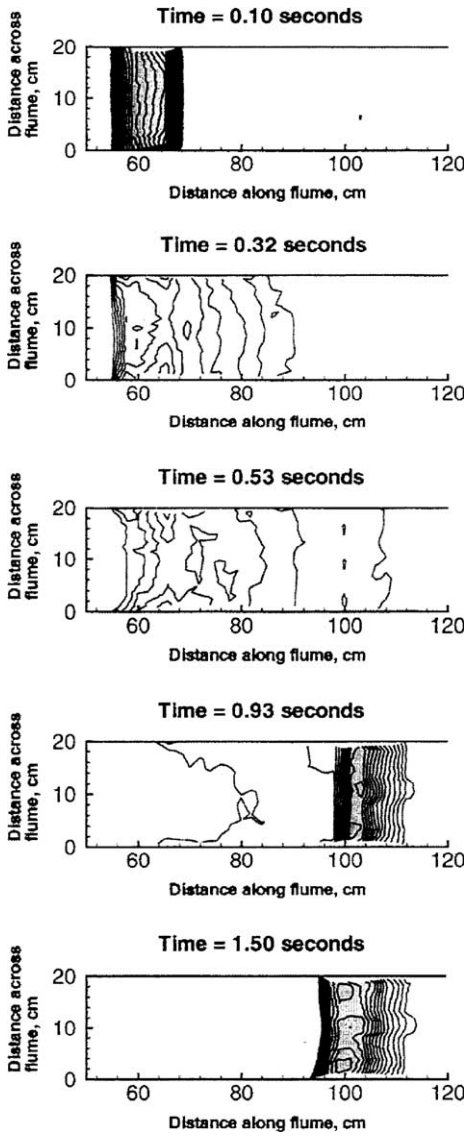

Fig. 5. Flow height results of the laboratory flume experiment done by Denlinger and Iverson [3]. Contours depict 1-mm isopachs of flow thickness normal to the bed.

granular flows in experiments III and V correspond to the shape of a hemispherical shell or a cap with a total volume of 290 cm^3 and the center at $(x_c|y_c) = (0.59|0.0)$

$$h(x,y) = \begin{cases} 0.0265\left(1 - \frac{(x-x_c)^2}{0.01} - \frac{(y-y_c)^2}{0.0049}\right) : & \frac{(x-x_c)^2}{0.01} - \frac{(y-y_c)^2}{0.0049} < 1. \\ 0 : & \text{else.} \end{cases}$$

In experiment IV where the dry granular flow is diverted by an obstacle, the inclined plane has the same inclination angle $\boldsymbol{\Theta}(x,y) = (\Theta_x, 0, 0)^{\mathrm{T}}$ as in experiment II. The obstacle has the shape of an obelisk, the center is located at $(x_c|y_c) = (0.2|0.0)$. The ground (gr) and the top (tp) faces have the dimensions

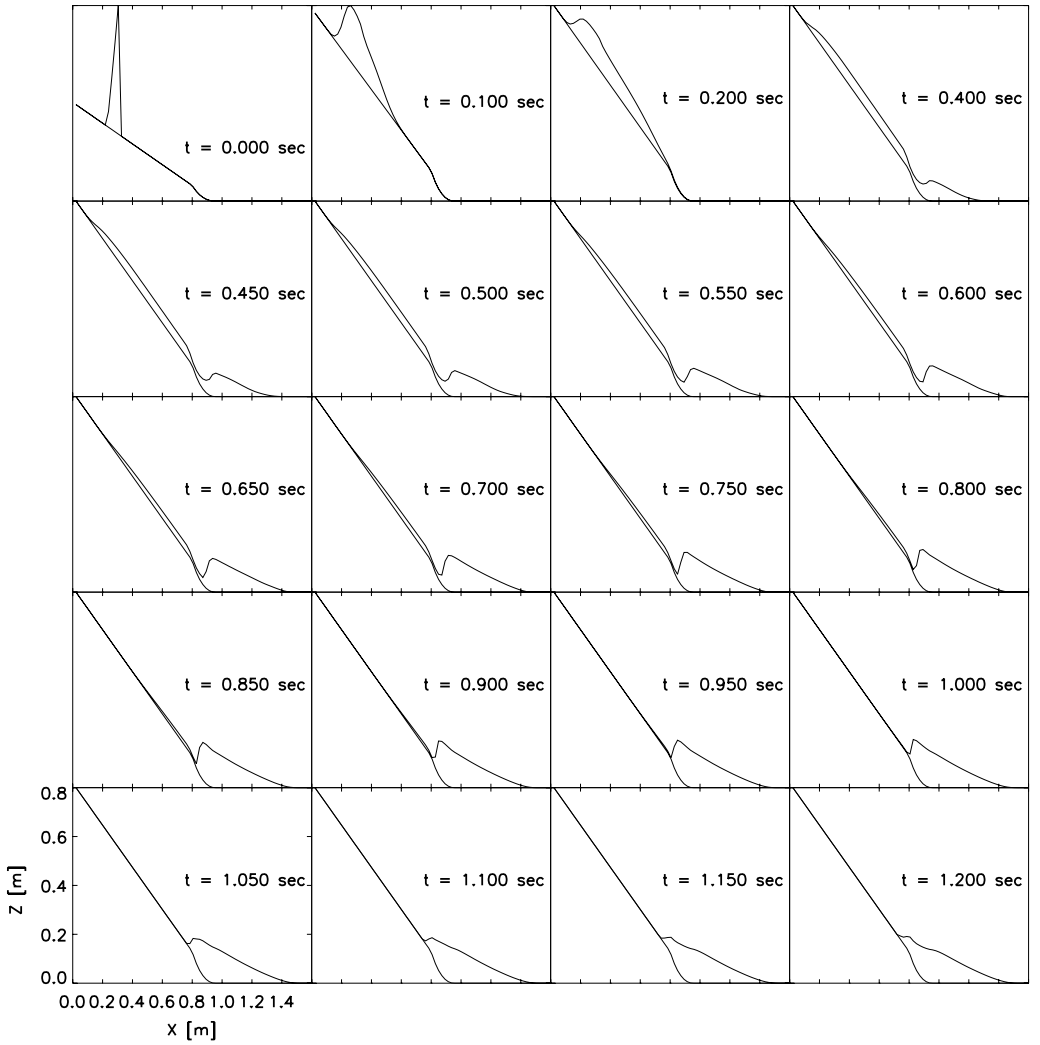

Fig. 6. Vertical slice (x–z) representation of the dry granular mixture flow height of the rectangular-flume experiment computed with the wave-propagation method. The rectangular flume consists of an inclined region ($x < 0.8$) with inclination angle $\Theta_0 = 40°$, a horizontal runout ($x > 0.95$) and a smooth transition region in between ($0.8 < x < 0.95$). The flow height on the bed surface is multiplied by a factor of 3 for a better visualization. The scale on the ordinate changes between the first and the other timeslices.

$x_{\mathrm{gr}} \in [0.465, 0.535] \times y_{\mathrm{gr}} \in [-0.035, 0.035]$ and $x_{\mathrm{tp}} \in [0.476, 0.523] \times y_{\mathrm{tp}} \in [-0.023, 0.023]$, respectively. The total height of the obelisk is $z_{\mathrm{tot}} = 0.6$. The position of the cap and the initial flow height are $(x_{\mathrm{c}}|y_{\mathrm{c}}) = (0.2|0.0)$,

$$h(x,y) = \begin{cases} 0.07\left(1. - \frac{(x-x_{\mathrm{c}})^2}{0.01} - \frac{(y-y_{\mathrm{c}})^2}{0.0049}\right) : & \frac{(x-x_{\mathrm{c}})^2}{0.01} - \frac{(y-y_{\mathrm{c}})^2}{0.0049} < 1, \\ 0 : & \text{else.} \end{cases}$$

The mass starts in all experiments from rest, so the initial condition for the velocity is $\mathbf{v} = (0,0,0)^{\mathrm{T}}$. The boundaries are closed at the sides parallel and open at the sides rectangular to the downslope or flow direction. There is no interstitial fluid assumed for the dry granular flow hence there must be no pore-pressure

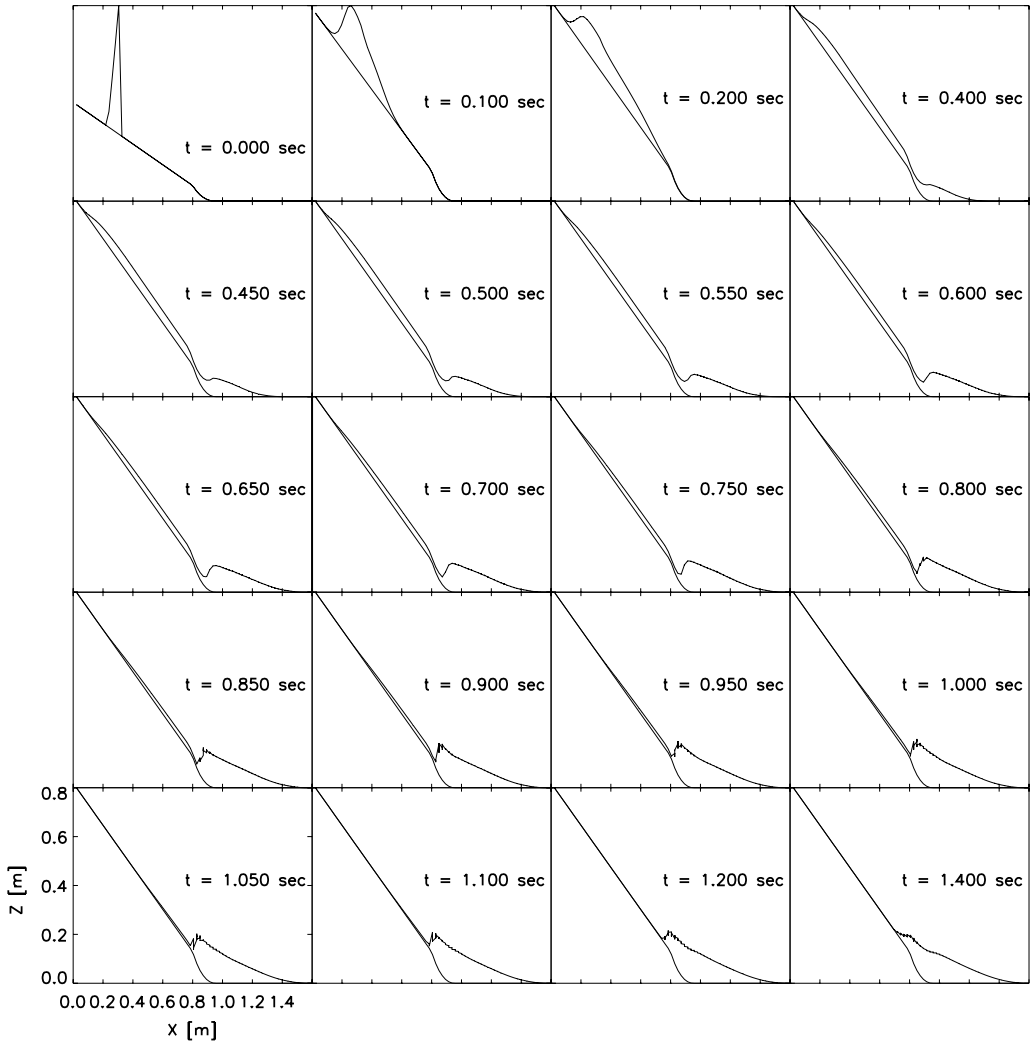

Fig. 7. Vertical slice (x–z) representation of the dry granular mixture flow height of the rectangular-flume experiment computed with the fractional-step method. The rectangular flume consists of an inclined region ($x < 0.8$) with inclination angle $\Theta_0 = 40°$, a horizontal runout ($x > 0.95$) and a smooth transition region in between ($0.8 < x < 0.95$). The flow height on the bed surface is multiplied by a factor of 3 for a better visualization. The scale on the ordinate changes between the first and the other timeslices.

considered, whereas in the case of the fluid-saturated granular flow it dominates the dynamical behaviour in the initiation phase and hence Eq. (5) has to be solved as proposed by [16]. The characteristics of the dry and the saturated material mixtures as proposed by [3] are shown in Table 1.

The subject of this numerical experiments is the evaluation of the influence of the two numerical schemes mentioned at the beginning of Section 4, on the computational results of the flowing and stopping behaviour, the shape of the depositions and the total propagation lengths. The computations are carried out on a numerical grid with 400 grid cells in x- and 100 in y-direction. The applied methods are of first order accuracy. This might lead to results which are smeared out compared to second order results, nevertheless the focus lies on a comparison of the first order results computed on the mentioned relatively fine numerical grid.

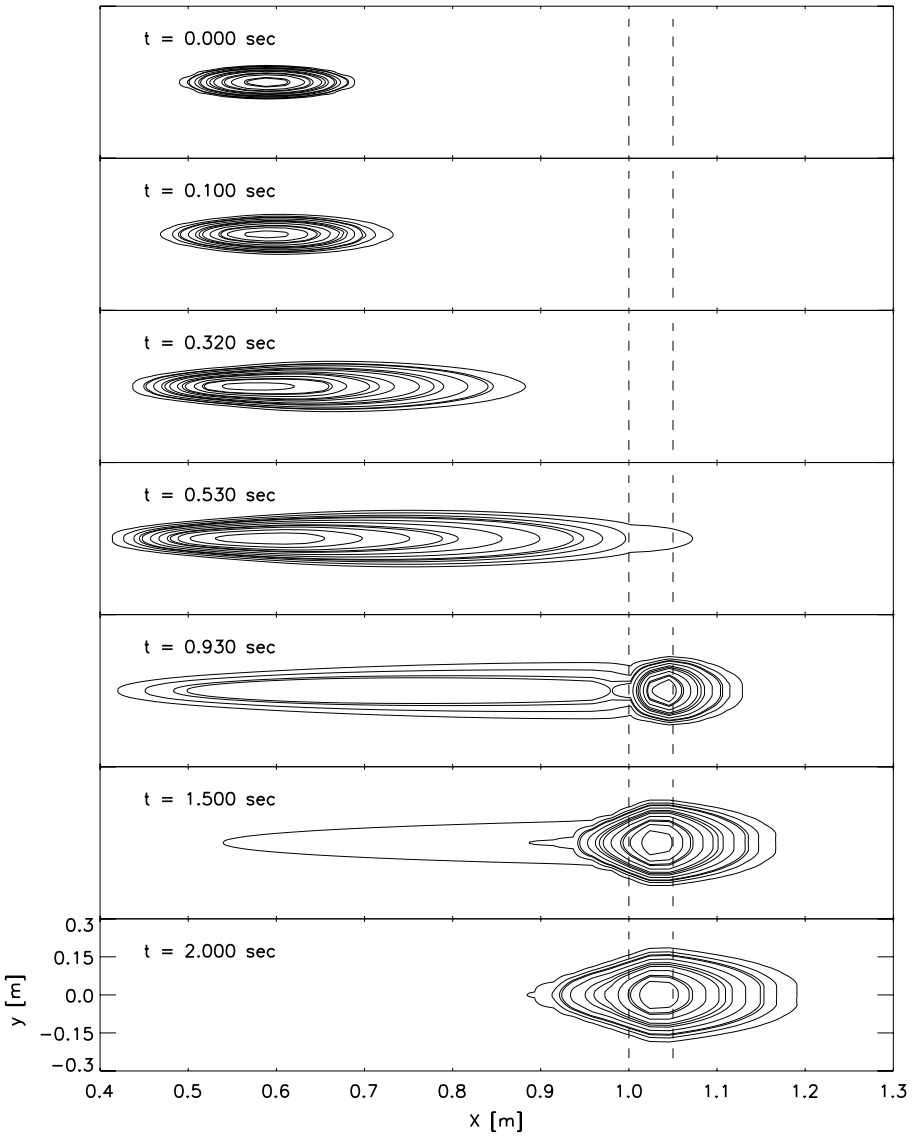

Fig. 8. Flow height results of the dry granular mixture of the inclined-plane experiment, computed with the wave-propagation method, as isoline representation. The inclined plane consists of an inclined region ($x < 1.0$) with inclination angle $\Theta_0 = 31.4°$, a horizontal runout ($x > 1.05$) and a smooth transition region in between ($1.0 < x < 1.05$). Contours depict 1-mm isopachs of flow thickness normal to the bed.

4.3. Numerical results and discussion

In all experiments the material mixtures are suddenly released at time $t = 0$. The bulk material starts to slide down the inclined plane, passes the transition region and comes to rest in the horizontal runout zone.

In the following all results are shown for both applied methods. Additionally the contours in the isoline representations depict 1-mm isopachs of flow thickness normal to the bed and the flow heights on the bed surface presented in the vertical slices are multiplied by a factor of 3 for a better visualization.

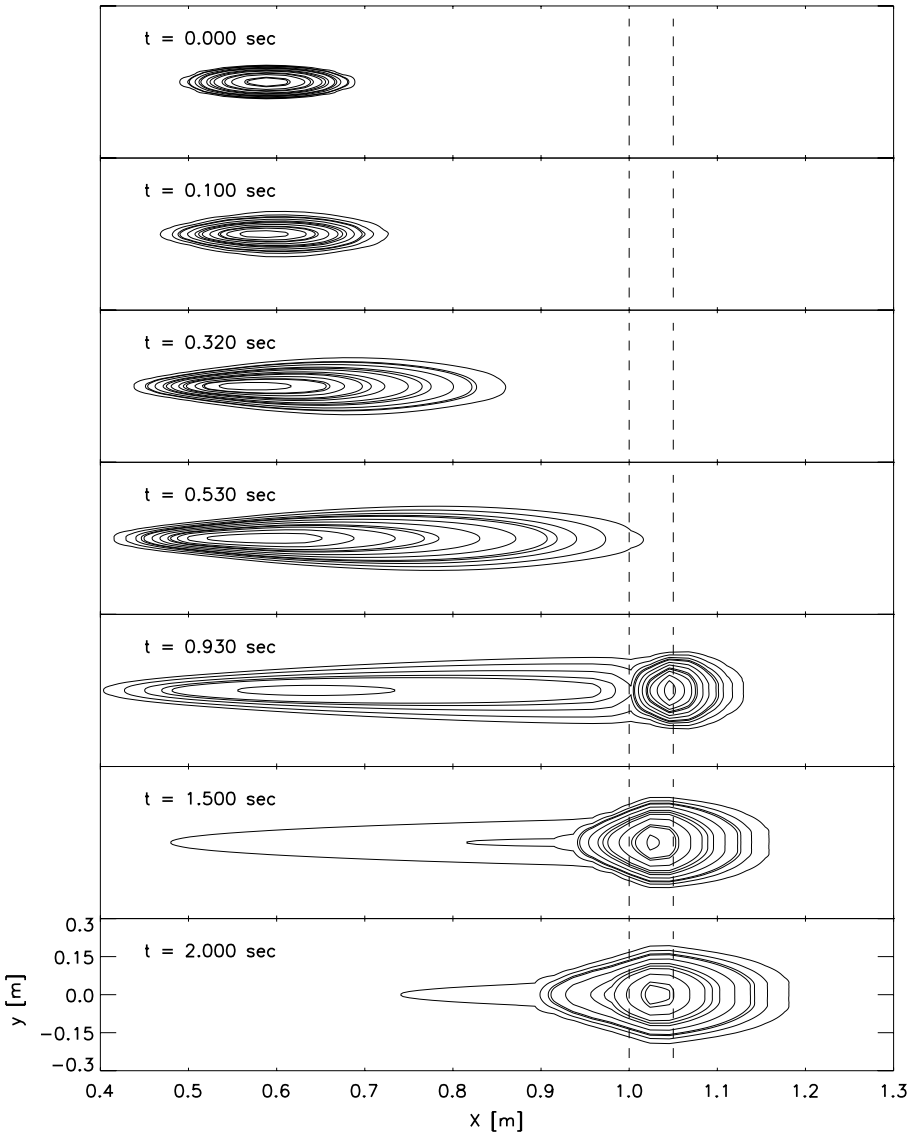

Fig. 9. Flow height results of the dry granular mixture of the inclined-plane experiment, computed with the fractional-step method, as isoline representation. The inclined plane consists of an inclined region ($x < 1.0$) with inclination angle $\Theta_0 = 31.4°$, a horizontal runout ($x > 1.05$) and a smooth transition region in between ($1.0 < x < 1.05$). Contours depict 1-mm isopachs of flow thickness normal to the bed.

Figs. 3 and 4 show the simulation results for the flow heights of experiment I at seven timeslices for both applied schemes as an isoline representation (left) and a vertical slice (x–z) representation (right). The comparison with results of a laboratory experiment done by Iverson and Denlinger [3] and presented in Fig. 5 reveals a significantly high agreement between the wave-propagation, the fractional-step and the laboratory results until $t = 0.53$ s. After 0.53 s there is a higher agreement between the laboratory and the wave-propagation results which even increases after 0.93 s. In the laboratory experiment the material completely comes to rest after 1.5 s and exhibits a sharp gradient in the upflow direction and a smooth flow

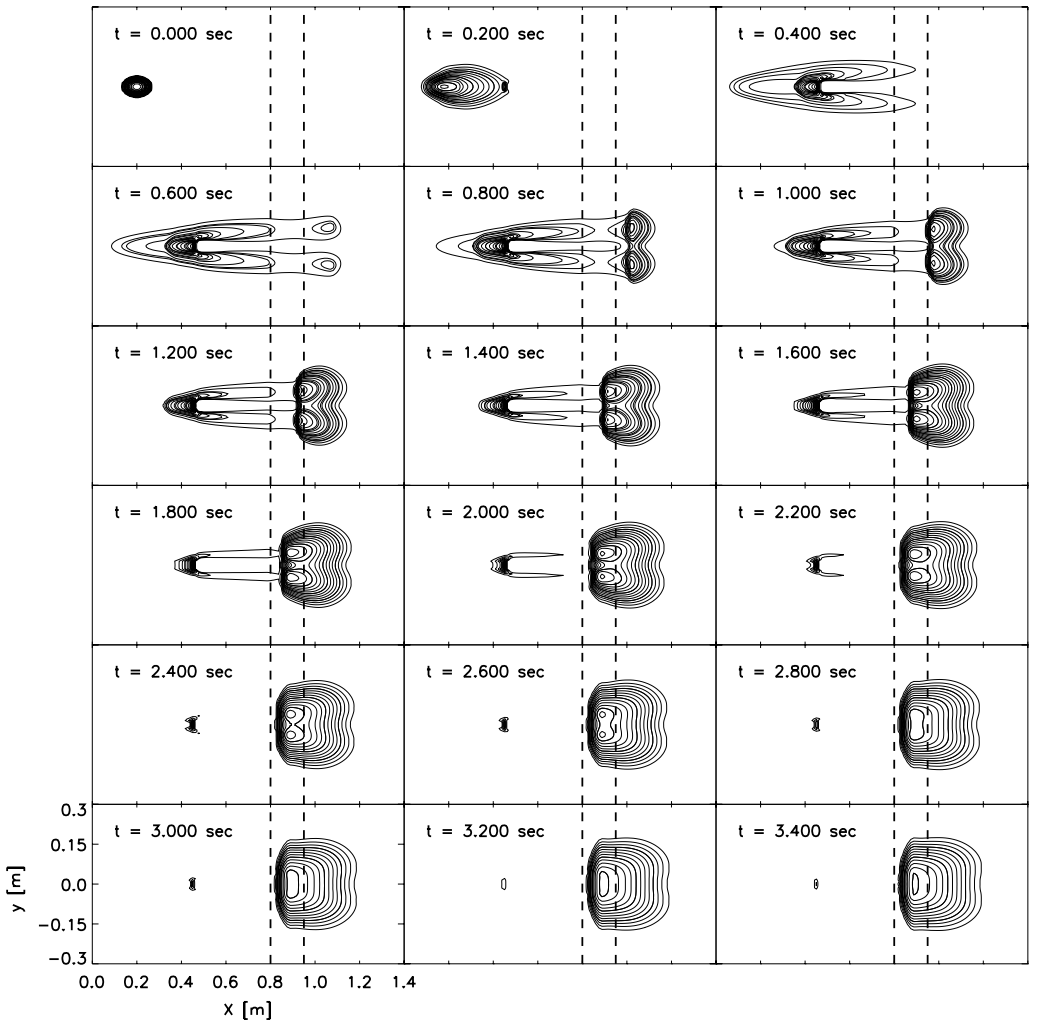

Fig. 10. Flow height results of the dry granular mixture for the inclined-plane experiment, computed with the wave-propagation method, as isoline representation. The inclined plane consists of an inclined region ($x < 0.8$) with inclination angle $\Theta_0 = 40°$, a horizontal runout ($x > 0.95$), a smooth transition region in between ($0.8 < x < 0.95$) and an obstacle located in the inclined region, which diverts the flow. Contours depict 1-mm isopachs of flow thickness normal to the bed.

height decrease in the down flow direction. The wave-propagation results show that after 1.5 s there is still a slight downflowing motion, which differs from the lab experiments, but the material completely comes to rest between 1.5 and 2.0 s. The reason might be that the Coulomb friction model which describes the stoppage of the material does not exactly reflect the natural conditions. It is a constitutive relation with a heuristic motivation, since the applied earth pressure coefficient $k_{a/p}$, introduced by Savage and Hutter [25], describes a discontinuous behaviour depending on the velocity gradient. It reaches the maximum for $\frac{\partial \bar{u}}{\partial \hat{x}} > 0$ and in the case of small flow heights like in the tail margins this causes an unphysically strong flow resisting force (3) and (4) and hence too small down flow velocities for the 'tail material'. Despite these shortcomings the model works quite resonable because the results show a significant flow height gradient in the upflow direction and a smooth flow height decrease in the down flow direction and hence the flow height behaviour

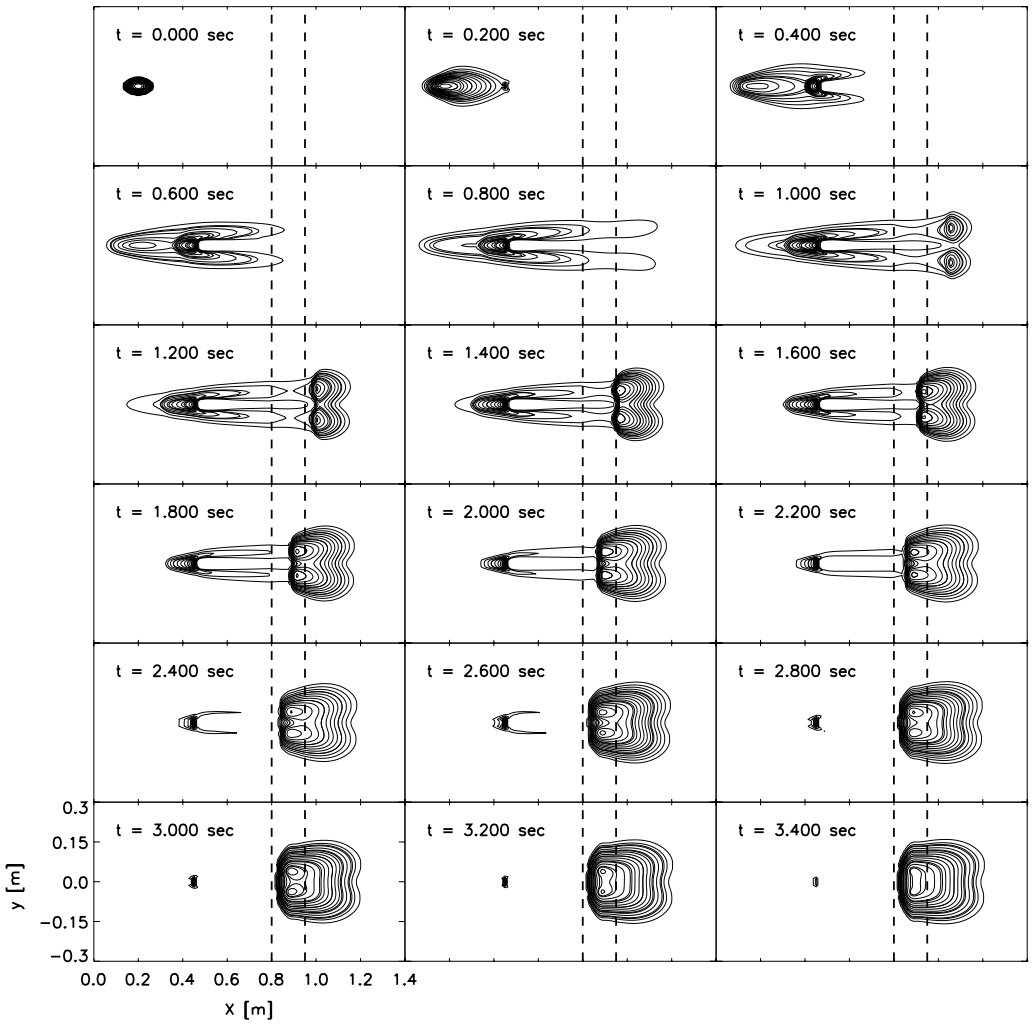

Fig. 11. Flow height results of the dry granular mixture for the inclined-plane experiment, computed with the fractional-step method, as isoline representation. The inclined plane consists of an inclined region ($x < 0.8$) with inclination angle $\Theta_0 = 40°$, a horizontal runout ($x > 0.95$), a smooth transition region in between ($0.8 < x < 0.95$) and an obstacle located in the inclined region, which diverts the flow. Contours depict 1-mm isopachs of flow thickness normal to the bed.

almost completely agrees with the lab experiments except for the tail margin. In the fractional-step case there is still some downflowing motion after 2.0 s, indicating a worst bulk velocity and the deposited material exhibits worst gradients in the upflow and the down flow direction compared to the wave-propagation results.

The results of the second experiment, shown in Figs. 6 and 7 for 20 timeslices, exhibit the ability of the numerical schemes to resolve an upward propagating shock. Both schemes resolve it quite well, but the wave-propagation scheme presents a more realistic flowing behaviour. The fractional-step results show unphysically oscillations which originate from the gradients in the source terms in combination with the way how the source terms are incorporated into the scheme. Additionally the mixture bulk velocity is significantly higher and more realistic in the wave-propagation case as already seen in experiment I, with

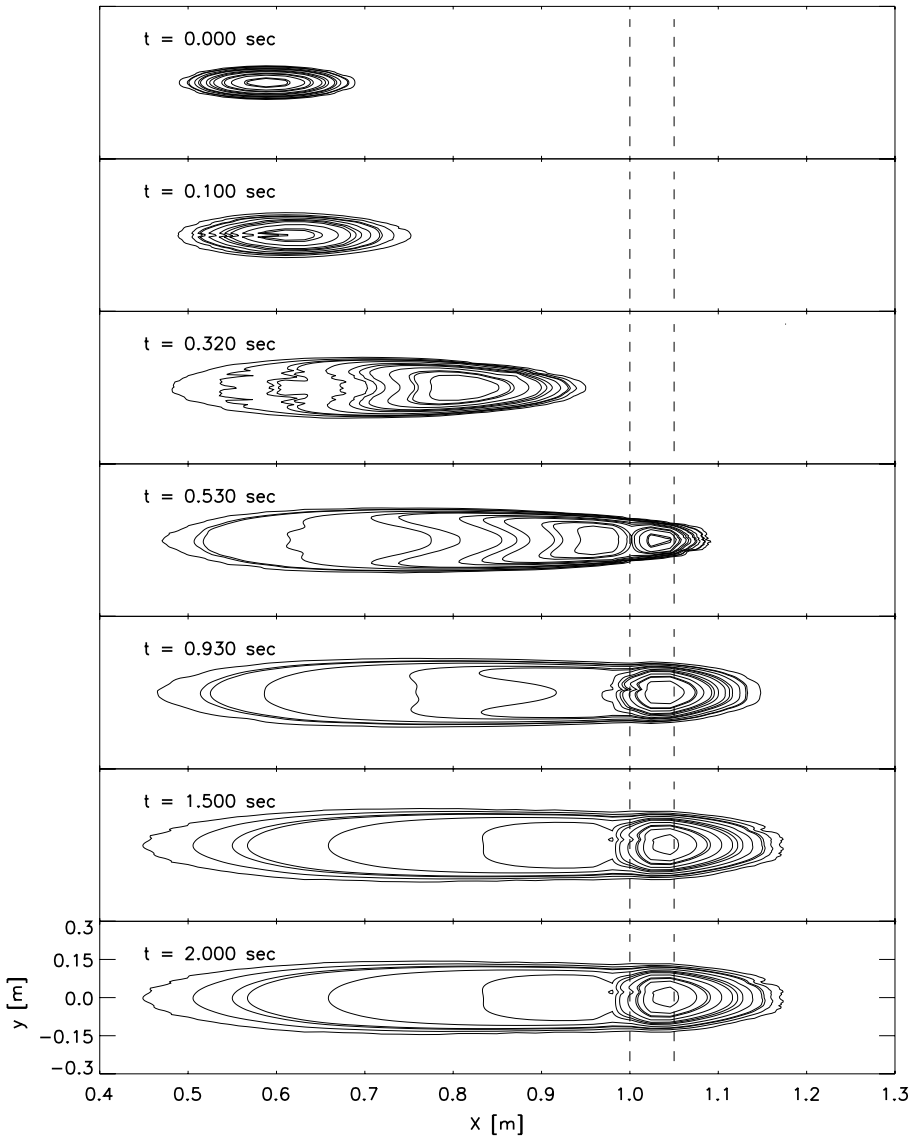

Fig. 12. Flow height results of the saturated granular mixture for the inclined-plane experiment, computed with the wave-propagation method, as isoline representation. The inclined plane consists of an inclined region ($x < 1.0$) with inclination angle $\Theta_0 = 31.4°$, a horizontal runout ($x > 1.05$) and a smooth transition region in between ($1.0 < x < 1.05$). Contours depict 1-mm isopachs of flow thickness normal to the bed.

the results that the shock starts to form after 0.4 s and it disappears after 1.05 s, whereas in the fractional-step case it starts around 0.55 s and disappears around 1.3 s.

Figs. 8 and 9 show the flow height results of experiment III. They basically show the same flowing and deposition behaviour than the 'quasi-one-dimensional' experiment I. In addition they show that both methods can cope with real two-dimensional situations and the qualitative comparison with laboratory experiments done by [24] reveals a realistic flowing and deposition behaviour.

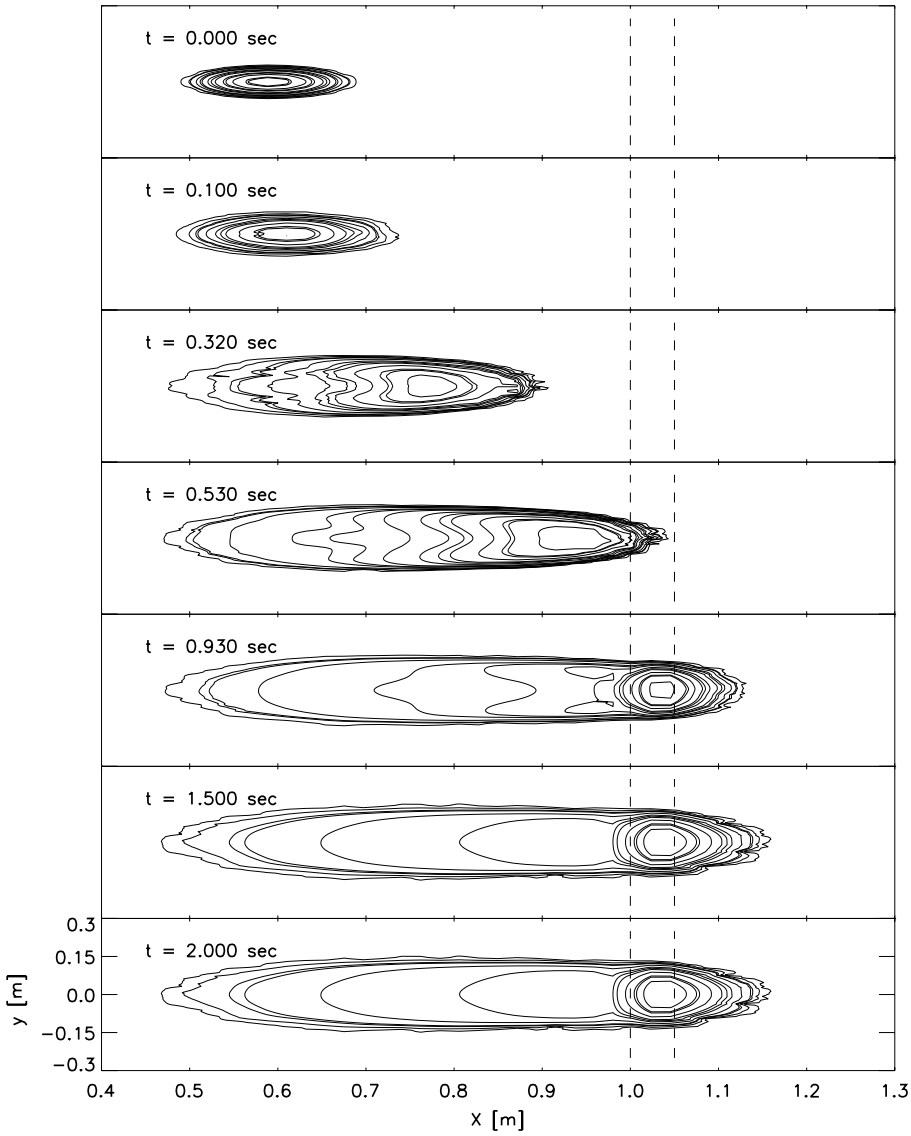

Fig. 13. Flow height results of the saturated granular mixture for the inclined-plane experiment, computed with the fractional-step method, as isoline representation. The inclined plane consists of an inclined region ($x < 1.0$) with inclination angle $\Theta_0 = 31.4°$, a horizontal runout ($x > 1.05$) and a smooth transition region in between ($1.0 < x < 1.05$). Contours depict 1-mm isopachs of flow thickness normal to the bed.

The results of experiment IV are shown in Figs. 10 and 11. In this experiment the flow is diverted by an obstacle being located on the inclined plane. They confirm the facts that on the one side the typical bulk velocity in the fractional-step case is significantly lower than in the wave-propagation case, which becomes transparent for example at timeslice 0.8 s because a lot more material has reached the runout zone in the wave-propagation case at this time. On the other side it must be mentioned that both methods as already seen in experiment III can cope with real two-dimensional situations. A qualitative comparison with second order results of [2] reveals a good qualitative agreement concerning the flowing and deposition behaviour.

In the experiment V the flowing and deposition behaviour of a completely saturated granular mixture down an inclined plane is computed. There seems to be no serious distinct between the two methods as shown in Figs. 12 and 13, except the fact that the typical velocities in the wave-propagation context are significantly higher. Both methods produce results which are influenced by the strong pore-pressure fluctuations, the derivatives and cross-slope derivatives and show a fringed behaviour.

The conclusion of the five computational experiments is that having the laboratory experiments done by Iverson and Denlinger [3] in mind, the wave-propagation method produces the more realistic results in terms of time-dependant flowing and deposition behaviour. The typical bulk velocity is higher than in the fractional-step case. The deposition behaviour which is dominated by the Coulomb friction approach, respectively, the constitutive relation is more realistic in the wave-propagation case, since the typical flow height gradients occurring in the deposited material show a greater agreement with the laboratory experiments. There is almost no distinct between the total propagation distances of the top margins computed with the two methods.

5. Conclusion

In this paper a shock-capturing wave-propagation method for the Savage–Hutter and the Iverson–Denlinger equations, which represent a generalization of the Savage–Hutter equations, was developed. These are systems of hyperbolic balance laws, taking the net driving force of the flow via source terms, representing the constitutive material relations, into account. These balance laws describe the time-dependent flow behaviour of dry granular or fluid-saturated granular flows e.g. debris flows over complex three-dimensional basal topography. The main purpose was the development of a numerical method for these equations which is based on a finite volume formulation and uses Godunov-type schemes, which guarantees a better balancing between the advection part and the source terms representing the net driving force of the material sliding than the classical fractional-step method. It additionally provides a solver immanent front tracking property. The discrepancy between the results computed with the classical fractional-step method on the one side and obtained through laboratory experiments on the other side requires such a development. The wave-propagation method developed by LeVeque et al. [21] for balance laws was adapted to the Iverson–Denlinger equations using a HLLC approximate Riemann solver. For a propagating flow front, where the wet/dry problem as described in Section 3.4 occurs, it operates on the basis of the exact Riemann solver and exhibits a solver immanent front treating property. The consideration of a solver being able to handle a front propagation was important because the determination of the exact front velocity is of importance for the quality of the results and hence requires a more sophisticated front tracking technique. The results are satisfying since the agreement between the computational results of the wave-propagation method and the laboratory results concerning the time-dependent propagation lengths, respectively, the propagation velocities and the deposition behaviour is very good and a lot higher than the agreement between the results computed with the fractional-step method and of the laboratory experiments.

Acknowledgements

I wish to thank Dick Iverson and Roger Denlinger for their inspiring work and many fruitful discussions. Furthermore, I am very thankful to the reviewers for their constructive and helpful comments. A part of the work was done during a stay at the Laboratory for Hydraulics, Hydrology and Glaciology of the ETH-Zürich (VAW).

References

[1] P. Arminjon, M.C. Viallon, Convergence of a finite volume extension of the Nessyahu–Tadmor scheme on unstructured grids for a two-dimensional linear hyperbolic equation, SIAM J. Numer. Anal. 36 (1999) 738.
[2] D.S. Bale, R.J. LeVeque, S. Mitran, J.A. Rossmanith, A wave propagation method for conservation laws and balance laws with spatially-varying flux functions, SIAM J. Sci. Comput. 24 (2002) 955–978.
[3] R.P. Denlinger, R.M. Iverson, Flow of variably fluidized granular masses across three-dimensional terrain: 2. Numerical predictions and experienced tests, J. Geophys. Res. 106 (2001) 553–566.
[4] E. Godlewski, P.-A. Raviart, Numerical Approximation of Hyperbolic Systems of Conservation Laws, Springer Verlag, New York/Berlin/Heidelberg, 1996.
[5] S.K. Godunov, A finite difference method for the computation of discontinuous solutions of the equations of fluid dynamics, Mat. Sb. 47 (1959) 357.
[6] J.M.N.T. Gray, Y.C. Tai, On the inclusion of a velocity dependent basal drag in avalanche models, Ann. Glaciol. 26 (1998) 37.
[7] J.M.N.T. Gray, M. Wieland, K. Hutter, Gravity-driven free surface flow of granular avalanches over complex basal topography, Proc. Roy. Soc. Lond. A 455 (1998) 1841–1874.
[8] R. Greve, K. Hutter, Motion of a granular avalanche in a convex and concave curved chute: experiments and theoretical predictions, Proc. R. Soc. Lond. A 445 (1993) 399.
[9] R. Greve, T. Koch, K. Hutter, Unconfined flow of granular avalanches along a partly curved chute. I. Theory, Proc. Roy. Soc. Lond. A 445 (1994) 399.
[10] A. Harten, P.D. Lax, B. van Leer, On upstream differencing and Godunov-type schemes for hyperbolic conservation laws, SIAM Rev. 25 (1983) 35.
[11] K. Hutter, Avalanche Dynamics, Lecture script, 2002.
[12] K. Hutter, Continuums Description of Granular Materials, Lecture script, 2002.
[13] K. Hutter, T. Koch, C. Plüss, S.B. Savage, The dynamics of avalanches of granular materials from initiation to runout, Acta Mech. 109 (1995) 127.
[14] K. Hutter, B. Svendsen, D. Rickenmann, Debris flow modelling: a review, Continuum Mech. Thermodyn. 8 (1996) 1–35.
[15] R.M. Iverson, The physics of debris flows, Rev. Geophys. 35 (1997) 245.
[16] R.M. Iverson, R.P. Denlinger, Flow of variably fluidized granular masses across three-dimensional terrain: 1. Coulomb mixture theory, J. Geophys. Res. 106 (2001) 537–552.
[17] D. Kröner, Numerical Schemes for Conservation Laws, Wiley-Teubner, Chichester/Stuttgart, 1997.
[18] R.J. Leveque, Wave propagation algorithm for multidimensional hyperbolic systems, J. Comput. Phys. 131 (1997) 327–353.
[19] R.J. Leveque, Balancing source terms and flux gradients in high-resolution Godunov methods: The quasi-steady wave-propagation algorithm, J. Comput. Phys. 146 (1998) 346–365.
[20] R.J. LeVeque, Finite Volume Methods for Hyperbolic Problems, Cambridge University Press, Cambridge, 2003.
[21] R.J. Leveque, D.E. Bale, S. Mitran, A. Rossmanith, A wave propagation method for conservation laws and balance laws with spatially-varying flux functions, J. Comput. Phys. (submitted).
[22] N. Nessyahu, E. Tadmor, Non-oscillatory central differencing for hyperbolic conservation laws, J. Comput. Phys. 87 (1990) 408.
[23] J.S. O'Brien, P.Y. Julien, Laboratory analysis of mudflow properties, J. Hydr. Eng. 114 (1988) 877–887.
[24] S. Pudasaini, Granular avalanche model in arbitrarily curved and twisted mountain terrain, Dissertation at the Technical University Darmstadt, 2003.
[25] W.Z. Savage, K. Hutter, The motion of a finite mass of granular material down a rough incline, J. Fluid Mech. 199 (1989) 177–215.
[26] W.Z. Savage, K. Hutter, The dynamics of avalanches of granular materials from initiation to runout, Acta Mech. 86 (1991) 201–223.
[27] Y.C. Tai, S. Noelle, J.M.N.T. Gray, K. Hutter, An accurate shock-capturing finite difference method to solve the Savage–Hutter equations in avalanche dynamics, Ann. Glaciol. 32 (2001) 263.
[28] Y.C. Tai, S. Noelle, J.M.N.T. Gray, K. Hutter, Shock-capturing and front-tracking methods for granular avalanches, J. Comput. Phys. 175 (2002) 269–301.
[29] E.F. Toro, Restoration of the contact surface in the HLL-Riemann solver, Shock Waves 4 (1994) 25–34.
[30] E.F. Toro, L. Francarollo, Experimental and numerical assessment of the shallow water model for two-dimensional dam-break type problems, J. Hydr. Res. 33 (1996) 843–864.
[31] E.F. Toro, Riemann Solvers and Numerical Methods for Fluid Dynamics, Springer, Berlin, 1997.
[32] E.F. Toro, Shock-Capturing Methods for Free-Surface Shallow Flows, Wiley, New York, 2001.
[33] Y. Wang, K. Hutter, S. Pudasaini, Savage–Hutter theory: a system of partial differential equations for avalanche flows of snow, debris and mud, submitted to ZAMM (2003).